University of Groningen

Bachelor's Thesis Project

Monte-Carlo Simulation of HPGe-Detector

Author:
Stephen Mulligan *(s3400255)*

Supervisors:
Dr. M. Kavatsyuk
Dr. J. G. Messchendorp

July 3, 2020

Abstract

In order to develop more advanced nuclear technologies, it is necessary to determine well the (n,xn) cross-sections of materials used in these technologies. As direct measurement of these cross-sections is difficult, gamma ray spectroscopy is used to determine (n,xnγ), which can then be used to determine (n,xn) cross-sections. HPGe detectors are used for gamma-ray spectroscopy, and Monte-Carlo simulations are employed to calibrate these detectors. This research performs a Monte-Carlo simulation of a HPGe detector with the aim of reproducing the energy spectrum of the detector in terms of energy resolution and efficiency. The results are inconclusive due to the poor quality of the measured ^{152}Eu spectrum as a result of a pile-up effect. Though inconclusive, analysis of results suggests a simulation with a better resolution than the detector, and a growth in the thickness of the detectors dead layer since its last calibration due to much higher efficiencies in the simulation at low energies.

Acknowledgements

Though it is difficult to do any particularly groundbreaking research during the course of a bachelor's project, it really is the culmination of a students entire degree, and so as well as thanking all the people who helped me complete this research project, I also need to thank those who helped get me keep going over the past three years. It has not always been easy or straightforward, but I am proud of this project and of the accomplishment that is finishing my BSc in Physics.

First of all, I must thank my first examiner and supervisor, Dr. Myroslav Kavatsyuk. Despite not being able to meet in person, he was always available to call when I needed to discuss a problem, and patiently explain the answers to questions I had, simple or complex. I appreciate him giving me the opportunity to work on this project, which depended hugely on coding in C++ to build the simulation, despite the fact that I had no experience using this language. Him having confidence that I could complete this work motivated me to work hard on developing the simulation, which seemed an insurmountable task at the beginning of this research.

Next, I must thank my second examiner Dr. Johan Messchendorp and all the other members of the Nuclear and Hadron Physics group for all the valuable feedback they provided on my research. In particular, I must thank Prof. Dr. Nasser Kalantar-Nayestanaki who put me in touch with Myroslav when I was first looking for a research project, and Dr. Catherine Rigollet, who provided valuable feedback after my first presentation on my research.

My family were key in supporting me through both this project and my degree. I would like to thank my parents, Brian and Caroline, who I moved back in with as a result of the COVID-19 crisis, and so they have had to put up with me during the entire project. I hope I was not too much of a pain or cost too much to feed. Thanks to my sister Eimear, for listening to me and sympathising with me when I complained about deadlines and error analysis.

I must also thank all my friends for support the help they provided. In particular, Briain Drew-Hartigan, who was always happy to explain how to do something in LaTeX or just call for a chat over a coffee when I needed a break. Tá sé orm cúpla deochanna a cheannach oíche amháin sa todhchaí ceapaim.

Finally, I must thank my wonderful girlfriend Stephanie Li, who has been with me through my whole degree and encouraged me throughout the course of this project. Thank you for keeping me sane, being there for me, and always believing me.

Contents

1 Introduction

1.1 Motivation

In this section the need for further research into nuclear energy technologies is discussed in the context of current and future global energy demands and the need for the reduction of carbon dioxide emissions to curb the damaging impacts of global warming.

1.1.1 Global Energy Needs and Global Warming

The International Energy Organisation(IEA) is an intergovernmental agency whose work focuses on "the enhancement of the reliability, affordability and sustainability of energy". According to their World Energy Outlook for 2019 almost one billion people still do not have access to electricity. Providing electricity to these people in the future will clearly necessitate an increase in energy production, though in order to avoid significant damage caused by climate change this increase in production must be pursued in a way such that any corresponding increase in greenhouse gas emissions is minimised[1].

The World Energy Outlook 2019 (produced by the IEA) describes three scenarios which outline how global energy needs could evolve over the next twenty years if different actions are taken (or not taken). The first, the current policy scenario, describes how global energy needs will carry on if current trends continue without change. It is expected that an increase in energy demand of 1.3% yearly will be reached, resulting in a continuous increase in energy production related emissions[1].

The second scenario, the stated policies scenario, describes the same development when world governments follow the specific policies they have already announced. In this scenario a 1.0% yearly rise in energy demand is expected. Though this slows the rise in emissions, global sustainability goals will not be reached by these policies alone, and a peak in global emissions will not occur before 2040[1].

The sustainable development scenario describes an approach for meeting sustainable energy goals in full. The goals of this scenario are inline with those set out by the Paris Agreement, to keep the rise in global temperatures "well below 2°C ... and pursuing efforts to limit [it] to 1.5°C"[2]. This is essential in order to minimise the damaging effects of global warming. The IPCC Special Report on Global Warming of 1.5°C, predicts with high confidence the " warming of extreme temperatures in many regions, and increases in frequency, intensity and/or amount of heavy precipitation in several regions". It also predicts with medium confidence "an increase in intensity or frequency of droughts in some regions". These are predicted for a global warming of 1.5°C as compared to pre-industrial levels[3]. All these effects are expected to be further exacerbated if warming reaches 2.0°. Keeping the rise in average global temperatures to global warming of 1.5°C instead of 2.0°C could result in "420 million fewer people being frequently exposed to extreme heatwaves... (medium confidence)". This would also "limit risks of increases in heavy precipitation

events in some regions" while also "reducing the probability of extreme droughts in other regions (medium confidence)"[3].

Such increases in global average temperature will most likely have a number of adverse societal impacts in terms of the damage or destruction of livelihoods, constraining economic growth and directly effecting human health[3]. All these impacts are projected to be less severe at a temperature increase of 1.5°C, and so it is imperative to limit warming to this temperature to avoid the instability and negative effects associated with any higher level of warming. In the sustainable development scenario proposed by the IEA in order to keep warming at 1.5°C, a model for global energy where "renewables account for around 80% of capacity additions in all regions" is described. This increase in capacity of renewables is supplemented by nuclear power and carbon capture technologies[1]. Further research into new nuclear energy technologies is therefore essential to achieve the goals of the Paris Agreement.

1.1.2 Modern Nuclear Energy

Currently, all commercial nuclear reactors in operation rely on uranium as their fuel source. The main design of these reactors are boiling water reactors and pressurised water reactors, which generate electricity by using the energy released from the fission of uranium nuclei to boil water and create steam which drives a turbine[4].

The World Nuclear Energy Association, as of May 2020, estimates that there are enough reserves of uranium available at competitive prices to last another 90 years[5]. Therefore if nuclear energy is to help with the global transition to a carbon free energy production model, it is necessary to develop other reactor types that utilise different fuel sources.

One potential alternative to uranium is the use of thorium(Th-232). Though Th-232 is not fissile, it is fertile, and so can be transmuted into uranium-233 , which is fissile. This transmuted U-233 can then be used as fuel for a reactor[6]. The viability of this thorium\uranium fuel cycle has already been demonstrated in the Canadian CANDU reactor[5]. Another type of reactor that has been proposed for using thorium fuel are molten salt reactors, where molten salt containing the fuel is used as the primary coolant[6].

In order to fully develop these new nuclear technologies, it is important that the behaviour of all materials used be well characterised. To achieve this, the inelastic and (n,xn) cross sections of these materials should be studied and understood.

1.2 Neutron Cross-Section Studies

A extensive neutron cross-section database is key to the development of new nuclear technologies, with neutron induced reactions being essential in the relation to nuclear power production. A detailed understanding of neutron cross-sections is extremely important to properly describe these neutron induced reactions[7].

In this section the role of the Geel Electron LINear Accelerator(GELINA) Neutron

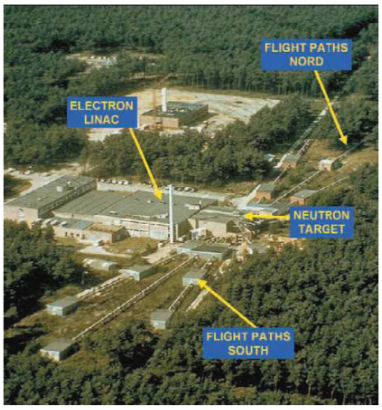

Figure 1: Aerial View of the GELINA time-of-flight facility from [7]

Time of Flight Facility in the investigation of inelastic and (n,xn) cross sections of materials relevant to nuclear technologies is discussed. The roles of both the Gamma Array for Inelastic Neutron Scattering (GAINS) and GeRmanium array for Actinides PrEcise MEasurements (GRAPhEME) are elaborated upon and linked to the topic of this research.

1.2.1 GELINA

As explained in the paper by D. Ene et al. [7], the GELINA Facility is a pulsed white neutron source for high resolution measurements using the time-of-flight technique. The four main components of the facility are a high-power pulsed linear electron accelerator, a post accelerating beam compression magnet system, a mercury cooled uranium target for neutron production, and the various flight paths along which different experimental setups are installed[8]. Figure 1 gives an aerial view of the facility, highlighting some of these important features.

According to the description given on the EU Science Hub [8] of the facility, "a typical beam operation mode for the linear electron accelerator uses 100 MeV average energy, 10 ns pulse length, 800 Hz repetition rate, 12 A peak and 100μA average current". The post-acceleration pulse compression system then reduces the pulse width to approximately 1 ns (FWHM), while maintaining the same current, which therefore produces a peak current of 120 A[8].

This compressed electron beam is then incident on the cooled uranium target. Uranium is well-suited to the production of photons via bremsstrahlung and so is selected to be used in the target, as when these photons are produced within the uranium target they will cause nuclear reactions, producing neutrons[7]. It is necessary to minimise neutron moderation by the coolant of the target, and mercury is well-suited to this role[7]. With the 1 ns pulse a peak neutron production of $4.3 \cdot 10^{10}$ neutrons can be obtained, with an average production rate of $3.4 \cdot 10^{13}$ neutrons/s. The neutron energy distribution of the produced

Figure 2: The GAINS Spectrometer[9]

neutrons covers a range from subthermal to 20 MeV, with its peak at 1-2 MeV. To obtain significant numbers of neutrons in the energy range below 100 keV it is necessary to add a hydrogen-rich moderator. It is then possible to select either moderated or unmoderated neutron beams for each flight path, depending on the energy range required for a certain experiment[8].

The flight paths are arranged symmetrically in a radial pattern about the uranium target. They range in length from 10 metres to 400 metres[8]. The flight tubes are under vacuum with a diameter of 50cm[7]. On each flight path experimental stations are installed. The two experimental setups that are of concern to this research are the GAINS and GRAPhEME setups.

1.2.2 GAINS and GRAPhEME

The GAINS setup is the experimental setup for the investigation of the neutron cross-sections of stable nuclei and is situated 200m from the the neutron source.

A fission chamber with ^{235}U deposits is placed in the neutron beam, before the location of the setup, for neutron flux determination. The samples have been carefully characterised by alpha counting to obtain the total activity and radial profile of the samples, which then allows the neutron flux passing through the fission chamber to be determined to within 2% uncertainty[9].

The GAINS spectrometer (figure 2) is composed of 12 high efficiency HPGe detectors placed about the target material, at 125°, 110° and 150° relative to the incoming neutron beam[9].

The remainder of the GAINS setup is composed of a classical acquisition system. This system is based on DC440 Acqiris 12 bit digitizers. This system is able to achieve neutron energy resolution of around 1 keV at 1 MeV and 3.5 keV at 10 MeV[9].

The GRAPhEME setup is the experimental setup used in the investigation of neutron

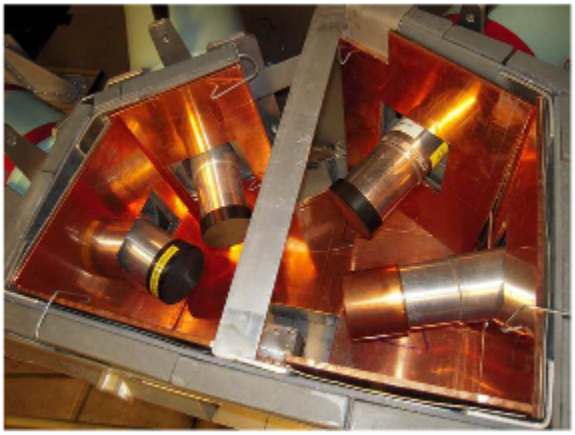

Figure 3: Top view of the GRAPhEME setup[9]

cross-sections of radioactive nuclei, or more specifically actinides. Compared to the GAINS setup, the flight path is significantly shorter, at 30m from the neutron source. This is in order to make up for the small amount of target nuclei used[9]. Conceptually, the GRAPhEME setup is analogous to the GAINS setup, though the details of the setup, like the length of the flight path, vary, as well as components used.

The neutron flux is again measured using a fission chamber employing ^{235}U samples placed in the beam, approximately 1 meter before the sample, which have been characterised in the same manner as the chamber used in the GAINS setup[9].

Four HPGe detectors (figure 3) are placed at 110° and 150° relative to the incoming neutron beam direction. It is important to note that since this setup is significantly closer to the neutron production source, the electronic devices used are sensitive to the electromagnetic field generated by the electron accelerator. To combat this, an electromagnetic insulation is added[9].

The data acquisition system associated to GRAPhEME is based on TNT2 card from the Institut Pluridisciplinaire Hubert Curien (IPHC). It has an amplitude resolution of 14 bits, and is able to achieve a neutron energy resolution of about 10keV at 1MeV and 1MeV at 20MeV[9].

In order to investigate the neutron cross-sections of the materials being studied in both of these setups, a technique known as *prompt γ-ray spectroscopy* is employed, which utilises the HPGe detectors common to each setup.

1.3 Prompt γ-Ray Spectroscopy

The study of (n,xn) cross-sections can be approached in different ways. The most direct method involves direct detection of emitted neutrons, but this requires the ability to distinguish between neutrons from elastic scattering, inelastic scattering, (n,xn) reactions, and,

if the sample is fissionable, neutrons produced in the fission process. This is difficult to achieve.

In order to avoid these issues, the technique of prompt γ-ray spectroscopy is employed at the GELINA facility. In this method, the γ emitted by the excited nucleus formed by the (n,xn) reaction is detected. It requires that the nuclear excitation scheme and the sample composition are well known, but if this is the case, the selective identification of detected γ-rays allows the reduction of the ambiguity to the underlying nuclear process. Angular differential (n,xnγ) cross-sections are measured for each transition, and when used in conjunction with the time-of-flight measurements that can be performed at the facility, an accurate description of the (n,xnγ) excitation function can be obtained. Incorporating information on branching ratios, conversion coefficients and level decay sequences, level production and total cross-sections can be determined, though the deduced total (n,xn) cross-section is often a lower limit[9].

In order to accurately utilise this technique, it is necessary to have well calibrated HPGe detector arrays. This can be aided through the simulation of these detectors, which is the aim of this research.

1.4 Simulation of HPGe Detectors

The goal of this research is to setup a Monte-Carlo (MC) simulation program which will reproduce the energy spectrum of a Germanium detector in terms of energy resolution and efficiency. MC simulations allow precise characterisation of the various data corrections to be achieved, and so attaining better control and determination of systematical uncertainty[9].

It had originally been planned to simulate the detector arrays from GELINA. These simulations would be validated with data sent from the facility. However, due to the ongoing COVID-19 crisis it was not possible to obtain calibration data for these arrays from the GELINA facility. Fortunately, there is a HPGe detector available to work with at KVI-CART in University of Groningen. HPGe detectors are relatively simple in design, and so aside from specific measurements and casing materials used, the detector at KVI-CART is thought to be sufficiently similar to those at GELINA. If a MC simulation program that reproduces well the energy spectrum from this HPGe detector can be designed, it is thought that it should be a relatively simple process to adjust measurements and materials of the simulated detector when data from the GELINA facility next becomes available.

The goal of this research is then to reproduce the energy spectrum for the HPGe detector located at KVI-CART in University of Groningen using MC-simulation methods. This will be done in terms of energy resolution and efficiency, and the results will be compared with data collected by the detector from calibration radioactive sources.

2 Theoretical Framework

2.1 Semiconductor Diode Detector

The behaviour of electrons in crystalline materials is described in terms energy bands, with a simplified model having two bands: valence and conduction. The valence band refers to energy levels at which electrons in the outer shells of atoms are localised at specific lattice sites within the crystal. The conduction band is made up of energy levels at which electrons move freely throughout the crystal. In semiconductors and insulators, these bands are separated by forbidden energy levels, which are referred to as the bandgap of the material. Semiconductors and insulators can be differentiated by the size of this bandgap, with semiconductors having a relatively narrow bandgap when compared to those of insulators[10]. These materials will then conduct electricity when a large enough voltage is applied so as to excite electrons into the conduction band.

When an electron is excited into the conduction band, it leaves a positively charged vacancy, known as a hole, in the valence band. These holes tend to move in an electric field, but in the opposite direction of to that of an electron, with the motion of both contributing to the conductivity of the material. The combination of both is known as an electron-hole pair. At any nonzero temperature, it is possible for a valence electron to gain sufficient thermal energy from other electrons in the valence band to be excited into the conduction band. The probability of an electron-hole pair being generated is related to the size of the bandgap and the absolute temperature by

$$p(T) = CT^{\frac{3}{2}} exp(-\frac{E_g}{2kT}) \tag{1}$$

where T is the absolute temperature, E_g is the bandgap energy, k represents the Boltzmann constant and C is a proportionality constant of the material[10].

In a semiconductor, electron-hole pairs move under the influence of an electric field , with a net drift velocity parallel to the direction of the applied field. This drift velocity is initially proportional to the strength of the applied field, however when the field strength becomes large enough, the *saturation velocity* is achieved, after which further increases in field strength will not produce corresponding increases in drift velocity. Semiconductor detectors are then generally operated with high enough field strengths to ensure that saturated drift velocity is achieved as this minimises the time required to collect the charge carriers and obtain a signal[11].

In addition to this drift, charge carriers are also subjected to the influence of random thermal motion that results in diffusion. Without this diffusion, all charge carriers would follow the paths of the electric field lines to the collecting electrodes of the detector. This diffusion causes a spread in arrival positions of charge carriers, and is well characterised by a Gaussian distribution with a standard deviation of

$$\sigma = \sqrt{\frac{2kTx}{e\mathcal{E}}} \tag{2}$$

with x the drift distance, $\mathcal{E}$ the electric field magnitude and e the charge of the electron. This spreading due to diffusion limits the precision that can be achieved for position measurements made using the location at which charges are collected at the electrodes of the detector[11].

Energy deposition occurs when incident radiation interacts in the active volume of a semiconductor. This energy deposition cause the creation of equal numbers of electrons and holes. Semiconductor detectors have a particular advantage here, with a relatively low ionisation energy (energy required to produce an electron-hole pair). For example, the value for germanium is about $3eV$ (see table 11.1 in [12]). This allows for a large number of charge carriers to be produced per unit energy deposited, and this large number of charge carriers reduces the impact of statistical fluctuations in the number of charge carriers produced. The reduction of the effect of statistical fluctuations therefore improves the obtained energy resolution, in comparison with other detector types[13].

2.2 Germanium Gamma-Ray Detectors Structure

The active volume of a semiconductor detector is approximately given by the volume of its depletion layer. For highly penetrating radiation such as gamma rays, it is important to have a large active volume in order to maximise the probability of an interaction. The thickness of the depletion region is given by

$$d = \sqrt{\frac{2\epsilon V}{eN}} \tag{3}$$

with V the reverse voltage bias, ϵ the dielectric constant, e the electron charge, and N the net impurity concentration in the bulk of the detector. Clearly, a larger active volume can therefore be achieved by reducing the net impurity concentration. Techniques for producing highly purified Germanium have been developed that can reduce the concentration of impurities to approximately $10^{10} atoms/cm^3$. Detectors produced from germanium of this purity are referred to as intrinsic or *high-purity germanium* (HPGe) detectors. While having the benefit of increasing the active volume of the detector, these HPGe detectors also have the advantage that it is only necessary to cool them during operation, unlike other types of germanium detectors which must be cooled constantly and can be damaged if they warm to room temperature[14].

The active volume of a germanium detector can be taken to be approximately the volume between the n^+ and p^+ contacts. Though thin relative to the size of the active volume, these contacts can be thick enough to contribute to a dead layer at the surface of the crystal, which can affect radiation on its way to the crystal. For gamma rays with energy values around 200 keV energy or greater, the impact of such layers can be is generally insignificant. The thickness of these dead layers can change slowly over time as a result of the formation of surface channels. As a result of this it is necessary to calibrate detectors regularly to determine accurately the thickness of its dead layers[15].

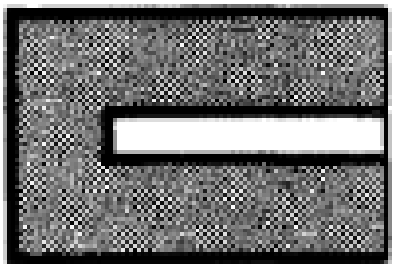

(a) Closed-ended coaxial configuration
Black lines represent electrical contacts

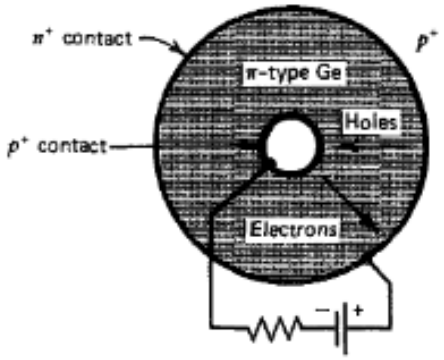

(b) High purity p-type coaxial detector

Figure 4: Closed-ended coaxial geometry [16]

Another contribution to the size of the active volume is the geometry of the detector. For HPGe detectors used in γ-ray spectroscopy, a *closed-ended coaxial* geometry is utilised. In this case, the outer surface of cylindrically shaped crystal is covered by an electrode, while the core of the crystal is removed so a second electrode can be placed in the inner surface of the crystal created by the core removal. By increasing the length of the crystal along the cylindrical axis, a larger active volume can be achieved while minimising the voltage necessary to form the depletion region. In some coaxial geometries, the central core is not fully removed with the outer contact extending over one flat end of the crystal (see figure 4a). This is employed to avoid complications arising from leakage currents at the front surface[16].

It should also be noted that for coaxial geometries, the rectifying contact can be placed either at the inner or outer surface of the crystal, which results in significantly different electric field conditions. In the case the rectifying contact is located on the outer surface, the depletion layer grows inwards until it reaches the inner hole surface at the depletion voltage. The opposite is true for a configuration with the rectifying contact on the inner surface, and a much larger voltage is required to fully deplete the detector volume. The first configuration results in higher electric field values in the outer volume of the crystal which is desirable as this is where most of the volume of the crystal lies. Because of these advantages, all coaxial HPGe detectors place their rectifying contact on the outer surface. The outer contact for a p-type HPGe (which is used in this research) will be n^+ (see figure 4b)[16].

2.3 Characteristics of Germanium Detectors

Germanium detectors are particularly useful when used for γ-ray spectroscopy due to the significantly better energy resolution that they achieve relative to other detector types that could be used, such as scintillator type detectors. This improved energy resolution helps

in the separation of peaks arising from transitions producing gamma rays of similar energy values. In other detectors these nearby transitions can be indistinguishable due the large width of the peaks.

The total energy resolution is mainly affected by three factors: the inherent statistical spread in the number of charge carriers, variations in charge collection efficiency, and contributions of electronic noise. At low energies, the contributions from electronic noise and charge collection are the most significant. The significance of the statistical spread in the number of charge carriers produced increases with increasing energy, and so an increase in spread is expected with increasing energy[17].

Though germanium detectors have improved resolution relative to other detectors, they suffer in terms of efficiency. Due to the smaller sizes available and lower atomic number(resulting in lower photoelectric cross-section), germanium detectors have photopeak efficiencies an order magnitude lower than corresponding scintillator detectors. The better resolution of germanium detectors does however offset this reduction in efficiency by helping with the identification of closely spaced and weak sources[18].

An important feature to note of the response function of a germanium detector is the presence of the Compton continuum. Though interactions are mostly photoelectric absorption for low-energy gamma rays, as the incident energy increases Compton scattering becomes more significant. Compton scattering in a detector will produce a characteristic Compton edge, which is an approximately normal distribution from the maximum energy transferred via Compton scattering to the minimum. At higher energy, events contributing to the photopeak are much more likely to be multiple interactions, such as Compton scattering followed by photoelectric absorption[18]. It should be noted that in this research incident gamma rays never have energy large enough for pair-production to become relevant[19].

2.4 Monte-Carlo Methods

A *Monte-Carlo Simulation*, otherwise known as a *stochastic computer simulation*, is defined as a simulation which incorporates some randomness in the underlying model, as opposed to a fully deterministic simulation[20]. These methods are used to perform simulations of physical systems which may be deterministic in nature, but current models do not well describe their behaviour. In this research the GEANT4 particle simulation toolkit is employed to build the simulation, which implements these techniques.

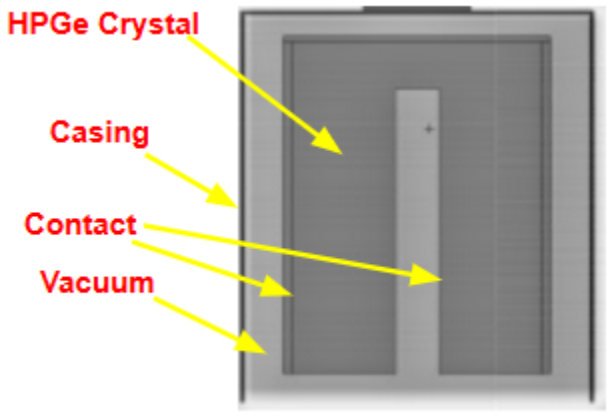

Figure 5: Labeled diagram of detector[21]

3 Experimental Setup and Simulation Method

Two measurements are made as part of this research. The first is of the gamma ray spectrum used for calibration of the ADC channels. This uses a ^{60}Co source was used in combination with a LYSO scintillator containing ^{176}Lu. The second measurement is taken using a ^{152}Eu source. The spectrum obtained from this is used to analyse the simulation output.

In this section, the simulation toolkit and design, the detector geometry, and the method for processing of the simulation output are described.

3.1 Detector Geometry

The detector used in this experiment is a closed-ended coaxial HPGe gamma detector (EG&G-Ortec, p-type, model GEM-45200-S). As of the last calibration of this detector, the germanium crystal has been found to have a diameter of 61.8 mm, a height of 78.3 mm, a 1.25 mm thick top dead layer (covering the closed-end) and a 2.1mm lateral dead layer (covering the length of the crystal). The detector is surrounded by a 1 mm thick magnesium end cap, with diameter 82.0 mm, height of 90.0 mm, and a 5 mm distance from the end cap to the crystal surface. The densities of germanium and magnesium were taken as 5.323 and 1.74 g cm^{-3} respectively[21]. The dead layers or contacts are diffused lithium of unknown density (standard density 0.534 g cm^{-3} from GEANT4 material is implemented in simulation[22])[23]. It should be noted that some of these measurements are not the nominal detector dimensions as provided by the manufacturer, but dimensions obtained from the calibration procedure as described by van der Graaf et al. in [21].

3.2 GEANT4

GEANT4 is a toolkit for simulating the passage of particles through matter. It provides precise simulation of electromagnetic interactions of particles with matter, covering a wide range of energies (from 250 eV to the TeV range). The toolkit exploits the benefits of object-oriented programming, and is implemented in the C++ programming language[24].

The toolkit allows for the creation of a geometrical model consisting of different shapes and components and to define "sensitive" elements that record information (hits) about a particles interaction with the model. The user is also able to control the characteristics of the generated primary particles, such as particle type, energy, and momentum and source distribution[24].

3.3 Simulation Description

Though there are many components necessary to construct a successful simulation, this description will focus on those key components necessary for a high level understanding of the simulation.

The geometry of the simulated detectors is in line with the description of the detector as described previously. The G4_Mg material provided in Geant4 matches the density of the end cap as described in[21] and so is used. The G4_Li material is also used for the dead layers as the density is unknown. Though the density of G4_Ge matches the provided density of the germanium crystal, the crystal must be cooled to liquid nitrogen temperatures (77K[15]) and so a user defined material is implemented. The detector is placed in a vacuum as the detector must be evacuated during operation (include values and source).

The two segments of the crystal (it was necessary to construct the crystal out of two volumes due to the partial hole in closed-ended coaxial detectors) are set as the sensitive detectors. These sensitive detectors generate hits and will record any non-zero energy deposition that takes place within the crystal of the detector.

The charge carriers and their collection at the contacts of the detector is not simulated. The thinking is that when energy deposition occurs, charge carriers are generated, and so this is what is recorded. The simulation of their movement and collection would add further complexity to the simulation. The characteristics of this process, as well as the characteristics of the electronics used to output the signal, can be taken from experimental measurements and reproduced by using a smoothing function on the simulation output.

The primary particle source is taken to be a point source, placed along the central(z) axis of the detector, 12.8 cm away. The primary particle is a gamma ray of user defined energy. The momentum of the primary particle is such as to always be heading along the z-axis, towards the detector, but with randomised x and y axis components. These randomised components are adjusted by inspection using visualisation of the detector and particle tracks so as to focus the majority of beams on the detector. This randomisation

of the x and y momentum components forms a "cone" of gamma rays. This is done to minimise time spent simulating particles that do not travel through the detector, and so reducing the run time of the simulation.

The energies of peaks in the measured spectrum are identified using a calibration function. The intensities of these peaks are found by matching these peak energies to transitions listed on the NuDat2 database from Brookhaven National Laboratory[25]. Using the ratios of these intensities, the number of events necessary to simulate each peak while maintaining the correct ratio between these peaks can be found.

The simulation outputs the recorded energy deposition in a .root file format so as to aid further processing and analysis, which is carried out in the ROOT data analysis framework. On its website, ROOT is described as "A modular scientific software toolkit. It provides all the functionalities needed to deal with big data processing, statistical analysis, visualisation and storage"[26]. It is primarily written in C++, with some integration with other languages.

3.4 Processing Simulation Output

This section describes the steps that are followed to further process the output after running of the simulation in GEANT4.

3.4.1 Calibration

The results of measurements taken with the detector are output in ADC channel numbers. It is therefore necessary to calibrate these ADC outputs by producing a function mapping ADC channel numbers to energy values.

To do this, measurements are taken of gamma ray sources with well known decay schemes. As the energy values of the gamma rays produced in these decays are well known, a function mapping the mean value of the peaks in the measured spectrum to their corresponding gamma ray energy can be produced.

For this research, a ^{60}Co source was used in combination with a LYSO scintillator containing ^{176}Lu. The decay schemes of both ^{60}Co and ^{176}Lu (figure 6a and 6b respectively) are well understood and cover the relevant energy ranges and so are well suited for calibrating the ADC channels. The most intense peaks from the decay schemes of each are listed in table 1[25].

The peaks on the ^{152}Eu spectrum are then fitted with gaussians to obtain their mean peak values and widths, and the calibration function is applied to these values to convert them into energy(keV) so the spectrum can be simulated.

3.4.2 Sigma as a Function of Energy and the Smoothing Function

As mentioned, contributions to the total width or sigma of a peak change as a function of energy. In particular, the contribution of the statistical spread in number of charge carri-

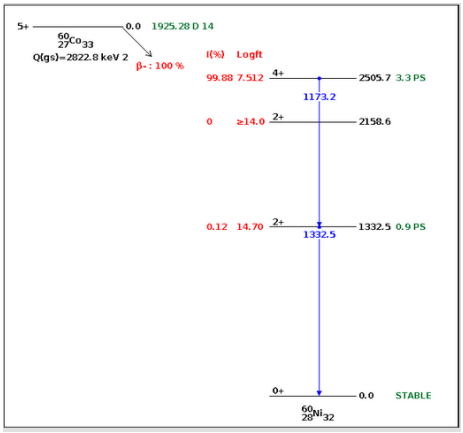

(a) ^{60}Co decay scheme

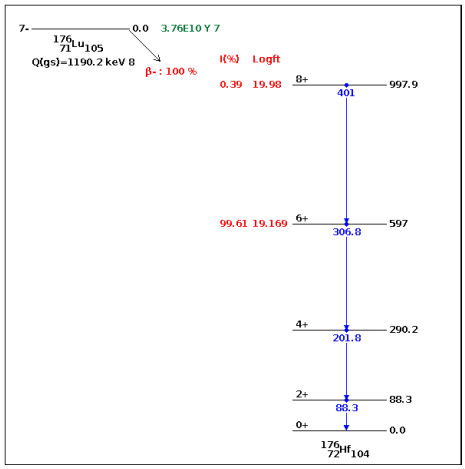

(b) ^{176}Lu decay scheme

Figure 6: Decay schemes of transitions used in calibration[25]

ers produced becomes more significant with increasing energy. Therefore a non-constant and increasing sigma as a function of energy is expected, though the exact behaviour is unknown.

To produce this function the sigma values of the peaks from the calibration spectrum from the calibration spectrum are used. The calibration spectrum again has the issue of having very few data points, making it difficult to infer any particularly complex behaviour. As the behaviour of sigma with increasing energy is expected to be increasing, but not necessarily linear, this could be a potential issue.

The mean peak values(keV) are plotted against their corresponding sigma values(keV) and a graph is fitted to these points. The parameters for this fit are then included in the smoothing function. This function takes a simulated peak .root file as its input. It takes the energy value of each point of the simulated peak, calculates its corresponding sigma value(using the previously obtained parameters) and then plots a point randomly from a gaussian with the energy value as its mean and the sigma value as its width. This causes a "smoothing" of the output of the simulation, and attempts to introduce sources of spread that the simulation does not account for.

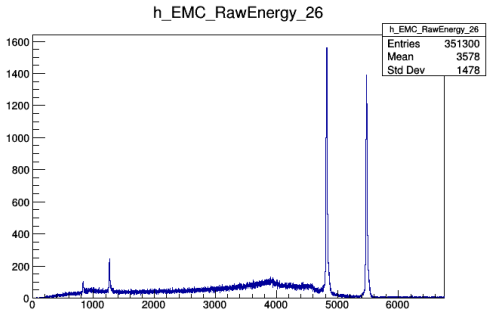

(a) ^{60}Co ^{176}Lu Calibration Spectrum

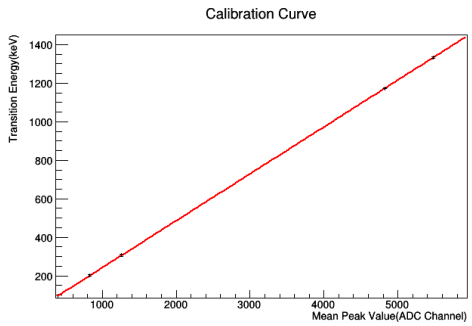

(b) Mean peak values vs transition energy

Figure 7: Mean peak values of recorded peaks for ^{60}Co and ^{176}Lu decay are plotted against corresponding transition energies to obtain calibration curve

4 Results

In this section, the results of each step of the simulation process are presented. Important plots and figures will be included. Any large tables and error analysis will be added in the appendix.

4.1 Calibration

An energy spectrum for ^{60}Co and ^{176}Lu with four distinct peaks is recorded(Figure 7a) and these peaks are fitted with gaussians in ROOT to obtain their mean peak values in the ADC channel outputs. The mean peak values are then plotted against their corresponding transition energy values (Table 1), and a linear plot is fitted to these points. The parameters of this linear plot are the parameters of our calibration function (Figure 7b). A linear fit is chosen due to the low number of data points, which makes it difficult to infer any more complex behaviour, and as the fit is within the error bars of each point. For this fit a slope of 0.2434(0.0009) and a y-intercept of -0.47 ± 3.02 is found.

Table 1: Table of relevant transitions, intensities, and their corresponding mean peak values

Element	Energy(keV)	Intensity(%)	Mean Peak Value (ADC Channel)
^{60}Co	1332.492 (4)	99.9826 (6)	5476.09 (7)
^{60}Co	1173.228 (3)	99.85 (3)	4821.90 (7)
^{176}Lu	306.78 (4)	93.6	1261.7 (2)
^{176}Lu	201.83 (3)	78.0 (25)	831.7 (4)

This calibration function is then used to convert the mean peak values, obtained by fitting the measured peaks with gaussians, of the ^{152}Eu spectrum (figure 8) from ADC

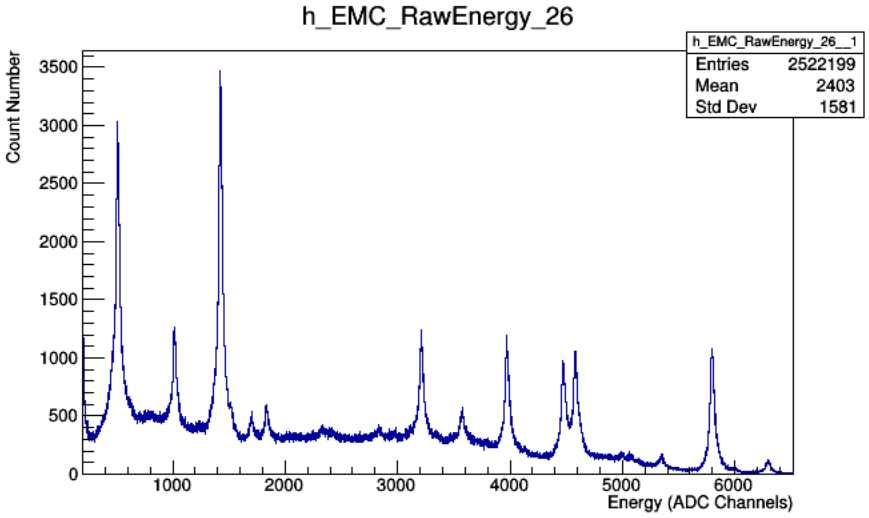

Figure 8: ^{152}Eu Measured Spectrum

channels to energy(keV). The ^{152}Eu decay radiation datasets on NuDat2 [25] are then checked to see if a corresponding transition exists, and its intensity is noted (Table 2). In total, 17 potential peaks were identified and fitted. This could be done for all but one of the peaks of the spectrum (peak number 4). The peak was very small, and so this indicates that it was arising from either Compton scattering, some other process associated with another peak on the spectrum, or a source of background radiation, but not a gamma produced by any transition associated with ^{152}Eu. It should also be noted that peak number 8 had two transitions of very similar value and intensity associated with it, and so when simulating the peak at this energy the sum of these intensity values is used.

4.2 Sigma as a function of Energy and the Smoothing Function

As well as mean peak values, sigma values from each peak are obtained for each peak of the ^{60}Co-^{176}Lu spectrum. Using the obtained calibration function, the sigma values in units of channel number are converted into energy(keV), and then plotted against their corresponding transition energy values. A linear plot is fitted to these points (figure 9), chosen for the same reasons as outlined for the calibration function. For this fit a slope of $6.6 \cdot 10^{-4} \pm 0.5 \cdot 10^{-4}$ and a y-intercept of 1.54 ± 0.06 is found, which is then used in the smoothing function.

4.3 Simulation

Using the corresponding intensities of each peak, the number of events at each energy to be simulated is determined. Peak 17, having the highest intensity, is chosen as the peak for

Table 2: Table of ^{152}Eu mean peak values and their matching transitions and intensities

Peak Number	Mean Peak Value (ADC Channel)	Converted Peak Energy (keV)	Matched Transition Energy (keV)	Intensity(%)
1	6294.8 (5)	1532 (7)	1528.1 (4)	0.279 (3)
2	5799.3(1)	1411 (6)	1408.013 (3)	20.87 (9)
3	5347.8 (9)	1301 (6)	1299.142 (8)	1.633 (11)
4	5076 (2)	1235 (6)	No Transition	None
5	4998 (1)	1216 (6)	1212.948 (11)	1.415 (8)
6	4584 (1)	1115 (5)	1112.076 (3)	13.67 (8)
7	4476.6 (2)	1089 (5)	1085.837 (10)	10.11 (5)
8	3973.5 (2)	967 (5)	963.38 (4)/964.057 (5)	11.6 (13)/14.51 (7)
9	3575.4 (5)	870 (5)	867.38 (3)	4.23 (3)
10	3212.0 (2)	781 (4)	778.9045 (24)	12.93 (8)
11	2829 (2)	688 (4)	688.67 (5)	0.856 (6)
12	2350 (7)	572 (4)	566.438 (6)	0.131 (3)
13	1836.0 (4)	446 (4)	443.9606 (16)	2.827 (14)
14	1702.5 (6)	414 (4)	411.1165 (12)	2.237 (13)
15	1425.80 (8)	347 (3)	344.2785 (12)	26.99 (20)
16	1017.2 (2)	247 (3)	244.6974 (8)	7.55 (4)
17	512.2 (1)	124 (3)	121.7817 (3)	28.53 (16)

which the maximum number of events, 1000000, will be simulated. The number of events N for every other peak is determined by

$$N = 1000000 \times \frac{Intensity\ of\ peak\ x}{Intensity\ of\ peak\ 17} \tag{4}$$

These values are listed in table 3. Each peak is then simulated separately and combined into a single histogram (figure 10a). This combined histogram is then passed through the smoothing function to obtain the simulated spectrum (figure 10b).

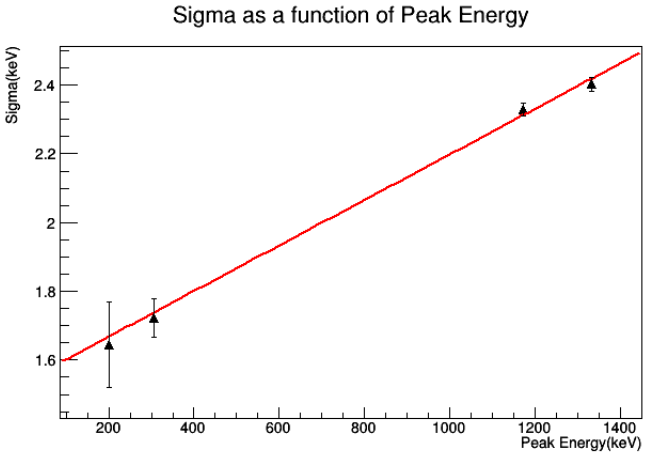

Figure 9: Plot of ^{60}Co-^{176}Lu sigma values as a function of peak energy

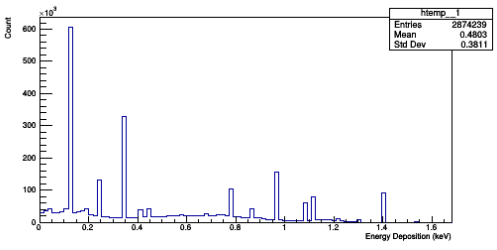

(a) Merged simulated peaks for ^{152}Eu

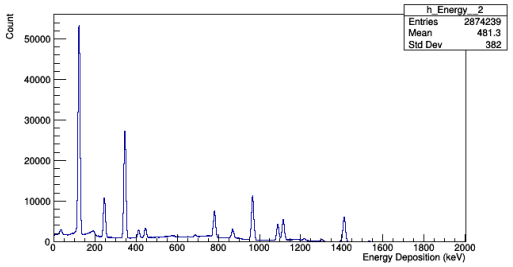

(b) Smoothed spectrum for ^{152}Eu

Figure 10: The action of the smoothing function on the simulated spectrum

Table 3: Relative intensity values used to calculate number of events to be simulated for each peak

Peak Number	Intensity Ratio	Events to be Simulated
1	0.009779179811	9779
2	0.7315106905	731511
3	0.05723799509	57238
4	No Transition	No Transition
5	0.04959691553	49597
6	0.4791447599	479145
7	0.3543638275	354364
8	0.9151770067	915177
9	0.1482649842	148265
10	0.4532071504	453207
11	0.03000350508	30004
12	0.004591657904	4592
13	0.09908867858	99089
14	0.0784086926	78409
15	0.9460217315	946022
16	0.2646337189	324634
17	1	1000000

4.4 Energy Resolution and Efficiency

To study the energy resolution of the simulation the sigma values of the widths of the simulated peaks are compared to those of the ^{152}Eu spectrum (see table 4). Initially, an attempt to fit a single gaussian to the peaks of this spectrum (like that of the calibration spectrum) was made.

It was found however, that the fit was extremely poor and was resulting in very large sigma values. It is thought that this is a result of a failure of the readout electronics due to a higher count rate associated with the ^{152}Eu source relative to those used in calibration. This high count rate results in a pile-up effect. In this case, a *tail pile-up* is observed, which impacts the quality of the resolution by "adding wings" to the peak[27].

To remedy this issue, a technique where two gaussians are fitted to the peak is employed. A narrow gaussian is fitted in order to remove the effect of pile-up on the resolution, while a second, wider gaussian is fitted so as to fit a curve to the entire peak. The sigma value for the peak is taken from the narrow peak. An example of this method is shown for a peak from the ^{152}Eu spectrum in figure 11.

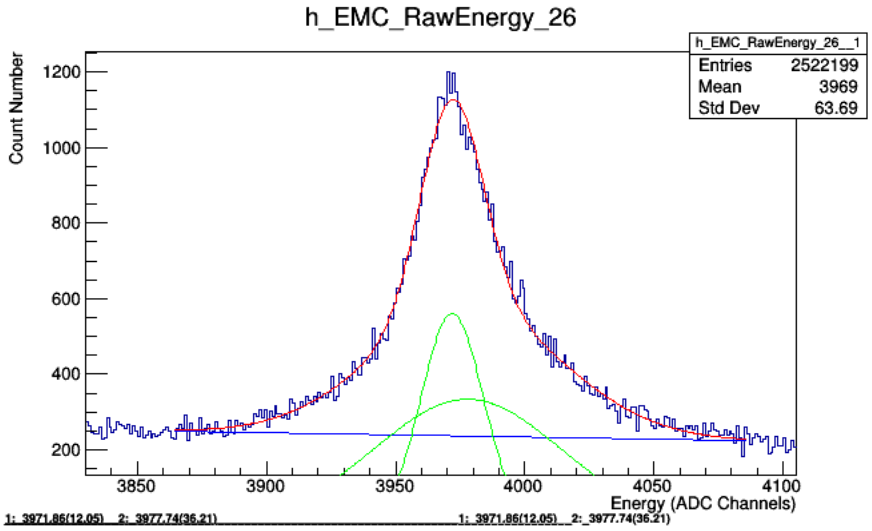

Figure 11: Fitting of two gaussians to peak

The peaks of the simulated spectrum are fitted with single gaussians, as the simulation does not replicate the pile-up and so the resolution of the simulation is not impacted in the same way. The ratio of the sigma values from the measured ^{152}Eu spectrum to the sigma values of the corresponding simulated peaks are plotted against peak energy(figure 12). Two fits are made: linear and constant. For the linear fit a slope of $-2.4 \cdot 10^{-4} \pm 0.3 \cdot 10^{-4}$ and a y-intercept of 1.62 ± 0.02 is found, while for the constant fit, a value of 1.45 ± 0.01 is obtained.

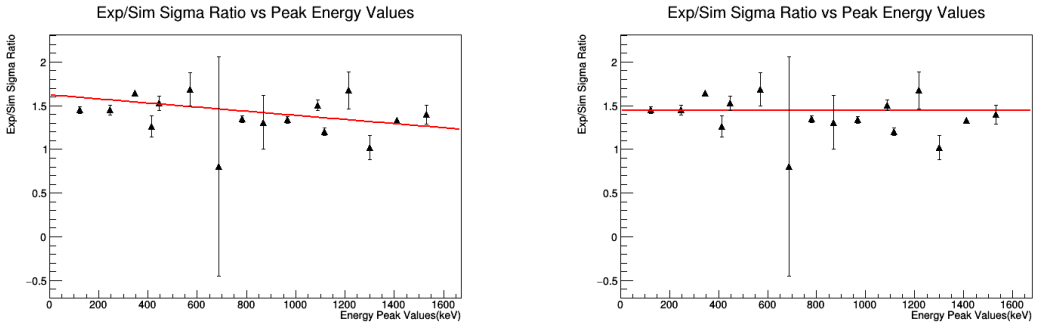

(a) Linear fit

(b) Constant fit

Figure 12: Fitted plots of sigma ratios against peak energies

To validate these fits a two sided chi-squared test is performed at significance level $\alpha = 0.05$. For the linear fit, $\chi^2 = 84.0835$, with number of degrees of freedom $\nu = 16 - 2 = 14$ (16 data points, 2 parameters fitted). Upper and lower critical values are 26.119 and 5.629 respectively[28], and so the linear fit is rejected. The constant fit has $\chi^2 = 170.971$ with $\nu = 15$. Corresponding upper and lower critical values are 27.488 and 6.262[28], rejecting this fit as well.

Table 4: Sigma and count values for both experimental and simulated spectra, and their ratios

Peak Number	Experimental Sigma (keV)	Simulated Sigma (keV)	Sigma Ratio	Measured Count Number	Simulated Count Number	Count Ratio
1	3.6 (3)	2.54(8)	1.4(1)	$4.4(2) \cdot 10^3$	$1.18(6) \cdot 10^3$	3.7(2)
2	3.32 (7)	2.499(6)	1.33(3)	$50.9(5) \cdot 10^3$	$91.9(4) \cdot 10^3$	0.555(6)
3	2.5 (3)	2.46(3)	1.0(1)	$3.5(2) \cdot 10^3$	$7.7(2) \cdot 10^3$	0.45(3)
4	3.8 (7)	No transition	No Transition	$1.5(2) \cdot 10^3$	No transition	No Transition
5	3.9 (5)	2.35(4)	1.7(2)	$2.0(2) \cdot 10^3$	$6.8(2) \cdot 10^3$	0.29(3)
6	2.8 (1)	2.298(8)	1.20(4)	$50.2(6) \cdot 10^3$	$70.9(4) \cdot 10^3$	0.71(1)
7	3.4 (1)	2.27(1)	1.50(6)	$39.8(5) \cdot 10^3$	$52.8(4) \cdot 10^3$	0.75(1)
8	2.95 (9)	2.204(5)	1.34(4)	$33.6(5) \cdot 10^3$	$148.9(6) \cdot 10^3$	0.226(4)
9	2.8 (7)	2.12(2)	1.3(3)	$9.1(4) \cdot 103$	$26.2(3) \cdot 10^3$	0.35(2)
10	2.77 (8)	2.060(8)	1.35(4)	$29.9(5) \cdot 10^3$	$84.9(5) \cdot 10^3$	0.352(7)
11	2 (3)	2.061(8)	0.80461±1.25459	$3.2(3) \cdot 10^3$	$5.8(3) \cdot 10^3$	0.55(6)
12	3.2 (3)	1.89(6)	1.7(2)	$9(3) \cdot 10^3$	$1.6(3) \cdot 10^3$	6(2)
13	2.8 (2)	1.83(2)	1.53(8)	$10.4(4) \cdot 10^3$	$27.2(3) \cdot 10^3$	0.38(2)
14	2.3 (2)	1.83(2)	1.3(1)	$6.4(4) \cdot 10^3$	$22.7(3) \cdot 10^3$	0.28(2)
15	2.93 (4)	1.788(3)	1.64(2)	$112.5(9) \cdot 10^3$	$312.8(9) \cdot 10^3$	0.360(3)
16	2.5 (1)	1.730(6)	1.45(6)	$28.0(6) \cdot 10^3$	$110.7(6) \cdot 10^3$	0.253(5)
17	2.38 (7)	1.642(2)	1.45(4)	$70.4(8) \cdot 10^3$	$56.9(1) \cdot 10^4$	0.124(5)

In order to investigate the efficiency of the simulation relative to the actual detector, we look at the number of counts recorded under each experimental peak, and then compare this number to the count number of the corresponding simulated peak (table 4). Specifically, the ratio of the experimental count number and the simulated count number is taken and is plotted against peak energy.

As before, a linear and constant fit are taken. For the linear fit a slope of $3.10 \cdot 10^{-4} \pm 0.04 \cdot 10^{-4}$ and a y-intercept of $1.12 \cdot 10^{-1} \pm 0.02 \cdot 10^{-1}$ is found. In figure 13 two plots are presented. Figure 13a is the full plot picturing all data points, while figure 13b gives an image without two large outliers, though these are still images of the same fit with all the same data points.

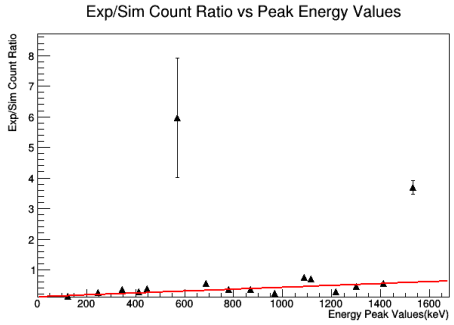

(a) Plot of count ratios against peak energy values

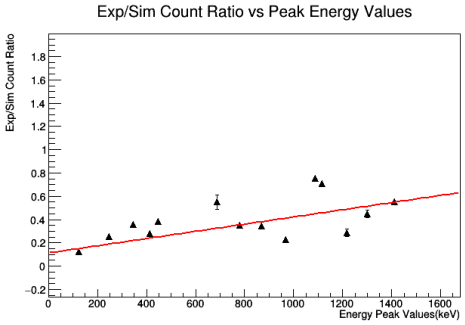

(b) Cropped plot of count ratios leaving out outliers

Figure 13: Linear fit of plot of count ratios against peak energy values, one enlarged to aide investigation

The corresponding constant fit for the count ratio gives a value of 0.209 ± -0.001, the plots shown in 14.

To validate these fits a two sided chi-squared test is again performed at significance level $\alpha = 0.05$. For the linear fit, $\chi^2 = 6467.57$, with number of degrees of freedom $\nu = 16 - 2 = 14$ (16 data points, 2 parameters fitted). Upper and lower critical values are 26.119 and 5.629 respectively[28], and so the linear fit is rejected. The constant fit has $\chi^2 = 15624.4$ with $\nu = 15$. Corresponding upper and lower critical values are 27.488 and 6.262[28], rejecting this fit as well. Both these fits seem exceptionally poor.

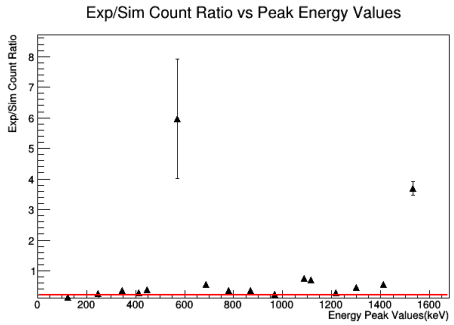

(a) Plot of count ratios against peak energy values

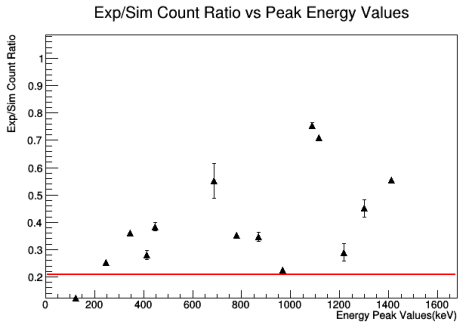

(b) Cropped plot of count ratios leaving out outliers

Figure 14: Constant fit of plot of count ratios against peak energy values, one enlarged to aide investigation

Table 5: Sigma values from multiple fittings of peak 8 and 10 using double gaussian method

Peak Number	Fit 1	Fit 2	Fit 3	Fit 4	Fit 5	Fit 6	Fit 7	Fit 8	Fit 9	Fit 10
8	11.2(4)	11.6(4)	11.2(5)	11.8(4)	11.5(3)	11.2(4)	11.3(4)	10.9(5)	12.1(4)	12.4(3)
10	11.3(3)	11.4(4)	11.5(3)	10.8(4)	11.4(4)	11.4(4)	12.6(5)	13.1(3)	13.0(4)	11.9(3)

4.4.1 Investigation of Failure of Fits

It was noticed that the sigma of the narrow gaussian fitted to peaks in the ^{152}Eu could change significantly due to variations in placement of boundary points used for the fitting of the gaussian. This could potentially lead to error in the sigma values resulting from the judgement of the user that is unaccounted for in the error value output. To investigate this, ten fits using the double gaussian method were made of two separate peaks of the ^{152}Eu spectrum, peak 8 and 10. The sigma values(ADC channel number) obtained from these fits are listed in table 5. The errors of the sigma values associated with the fitting of peaks used in the analysis of the performance of the simulation cover a range of values centred on the sigma value obtained from the original fit. For peak 8 this is 11.7 to 12.6 and 11.1 to 11.7 for peak 10, see table 6 in the appendix for these values. The sigma values of table 5 are checked to see if they fall within these ranges. Yellow colouring indicates the sigma value falls outside the range, but the range covered by accounting for its error overlaps with the previously described range. Red colouring indicates that even accounting for the error of the sigma value, it still falls outside the range.

As can be seen from table 5 30% of the values fall fully outside of their respective ranges, with 60% only having overlapping ranges. This suggests the potential for a reasonably large error resulting from the described issues with the fitting.

Making the assumption that 68% of the measured values should be within the range spanned by the error of the recorded sigma value, an increase of the error by ± 0.5 due to variations inherent in the fitting procedure can be justified.

For the linear fit a slope of $-1.8 \cdot 10^{-4} \pm 0.7 \cdot 10^{-4}$ with a y-intercept of 1.55 ± 0.07. A $\chi^2 = 16.0636$ is found which falls between the critical values for a two sided chi-squared test at significance level of $\alpha = 0.05$. The constant fit achieves a value of 1.40 ± 0.03 with a $\chi^2 = 22.65$, which the chi-squared test also fails to reject. The issue of having no acceptable fit has now been replaced with the inability to discriminate between both fits as the chi-squared test now fails to reject both. These plots are shown in figure 15.

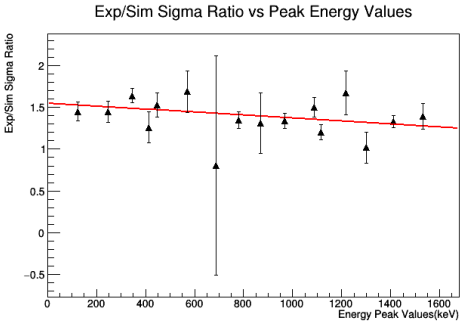

(a) Linear plot of sigma ratios against peak energy values

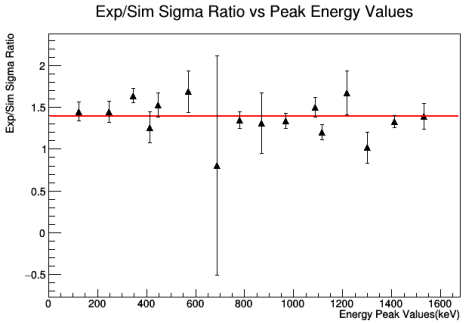

(b) Constant plot of sigma ratios against peak energy values

Figure 15: Adjusted error plots

This issue of non-constant error introduced by the double gaussian fit method is also suspected to lead to unaccounted for variation in the count ratio.

5 Discussion

The goal of this research was to simulate the energy spectrum of a HPGe detector in terms of energy resolution and efficiency. In this section, the extent to which this was achieved is discussed using the results presented in the previous section.

5.1 Energy Resolution

A perfect replication of the detector energy resolution by the simulation would output widths such that a constant ratio of 1.0 would be achieved. Here, an average ratio of approximately 1.3 is obtained. All but one of the sigma ratios are greater than 1.0, indicating that this simulation approach has failed to fully account for all factors contributing to the spread of peak energy values. The linear fit in figure 12a has a shallow slope of $-2.4 \cdot 10^{-4} \pm 0.3 \cdot 10^{-4}$, which would indicate that the sigma ratio is on average, constant. The small negative slope could indicate a slight increase in widths at lower energy levels as a result of increased noise at these low levels. Looking at figure 8, a large amount of electronic noise can be seen at lower energy levels, which decreases significantly with increasing energy.

It should be noted as the ^{60}Co-^{176}Lu spectrum used for calibration only has two relatively weak peaks at lower energies, it is possible that the smoothing function does not properly account for spreading that occurs at lower energy values when more intense transitions are present.

Though the shallow slope motivates the conclusion that the preferred fit for the sigma ratio is the constant fit, it should be remembered that it is effectively impossible to determine definitively the correct fit or behaviour of the sigma ratio plot due to the rejection of both fits by the chi-squared test. Conversely, it is also not possible to stat outright that the simulation fails to reproduce well the resolution of the detector, due to the poor quality of the ^{152}Eu spectrum resulting from the pile-up effect.

5.2 Simulation Efficiency

Analysis of the efficiency of the simulation when compared to the measured spectrum is a little less straightforward than for the energy resolution. Unlike the energy resolution where an ideal sigma ratio of 1.0 exists, no such corresponding ideal value is available for the count ratio as the number of events simulated is arbitrary. There is however, an ideal behaviour. In the case that the simulation perfectly reproduces the efficiency of the detector, it would be expected that the count ratios would be constant over the whole energy range.

For the fit in figure 13 a slope of $3.10 \cdot 10^{-4} \pm 0.04 \cdot 10^{-4}$ is found. Apart from two outliers, the ratios are all of comparable magnitude, though generally increasing with increasing energy. As the count ratio is given by measured count divided by simulated

count, this indicates a decrease in the efficiency of the simulated detector with increasing energy, though this slope is quite shallow.

Compare the ratio of recorded counts for peak 15 to peak 17 in both the measured and simulated spectrum. For the measured spectrum, $\frac{Peak\,15}{Peak\,17} = \frac{112540.0764}{70402.4372} \approx 1.6$, while for the simulated spectrum the same ratio gives $\frac{312840.862}{569323.0134} \approx 0.6$. This is quite a large discrepancy, particularly as these two peaks are the most intense in the spectrum.

A possible explanation for this issue is the thickness of the dead layers of the detector. As mentioned in section 2.2, the impact of dead layers only becomes significant for gamma ray energies lower than 200 keV. The transition energy for peak 17 is 124.199 keV (see table 2), making the thickness of the dead layers significant for this transition. Therefore this discrepancy is indicative of a thicker than expected dead layer, as a lower fraction of the simulated gammas at this energy are interacting with the dead layer, resulting in a significantly higher recorded count. The paper used for the geometry of the simulation [21] was published in 2014, and it is not unreasonable to think the thickness of the dead layer has increased since that calibration was performed.

The constant fit is extremely poor, and so it is very unlikely that the simulation reproduces well the efficiency of the detector. Much of this inaccuracy could again be linked to the detrimental impact of the pile-up effect on the recorded spectrum and issues with the method employed to remedy this. The spreading of peaks caused by the pile-up effect may lead to inaccuracies in determining the the true count number under each peak, and these errors may be non-constant due to variation introduced by the double-gaussian method used to fit these peaks. This non-constant error could then lead to the non-constant peak ratios seen.

Another potential source of error that should be mentioned is the matching of the smallest peaks to low intensity transitions. Some of the very small peaks had a large number of potential transitions. When the sum of these intensities were taken, intensity values comparable to significantly larger peak were achieved, which is obviously incorrect. A few transitions that best matched the calibration were then taken. If the simulation was to be repeated perhaps a cutoff value for peaks should be chose, peaks below which would not be simulated. It should be noted that excluding these peaks from the fitting of the plot has been tested and no significant improvement in the fit was observed.

6 Summary and Conclusion

The pile-up effect has a significant impact on the quality of the ^{152}Eu spectrum. The increased width makes it difficult to determine accurately the true widths of the peaks, and the variation introduced by the double-gaussian method used to combat this makes it impossible to definitively conclude if the simulation reproduces the energy resolution well. Any error introduced to account for this variation does not allow any conclusions to be drawn about the most appropriate fit, as neither is rejected by a chi-squared test.

The spreading of the peaks by the pile-up effect also causes issues with determining the how well the simulation reproduces the detector efficiency, by introducing non-constant error in the count number via the double-gaussian method.The generally increasing count ratio suggests a higher than expected efficiency at lower energy levels, potentially due to an increase in dead layer thickness, though again it is not possible to make any concrete claims due to the poor quality of the spectrum

On the whole, it is effectively impossible to make any definitive statements with regards to the success or failure of the simulation. Analysis of results suggests a constant sigma ratio of approximately 1.3, which would indicate a better resolution in the simulation than the detector, and an increasing count ratio which suggests higher efficiency at low energy levels in the simulation.

It should however be considered a success that a Monte-Carlo simulation framework for a HPGe detector has been designed that seems to output reasonable results, and hopefully can be used as a basis for further research.

Ultimately, the measurement of the ^{152}Eu spectrum should be repeated. The source should be placed further back from the detector, which would reduce the frequency of emitted radiation passing through the detector, in turn decreasing the count rate and reducing or eliminating the impact of pile-up on the spectrum. If the same increase in count ratio is still seen, the thickness of the dead layers in the simulation should be adjusted until a constant count ratio could be obtained. In this way, an updated value for the dead layer thickness could be obtained. Unfortunately obtaining a new spectrum measurement was impossible as a result of the current COVID-19 situation.

With regards to future extensions to this project, the ultimate aim is to simulate a full HPGe detector array from GELINA. If after obtaining a new spectrum for ^{152}Eu it can be shown that the simulation reproduces well the energy spectrum of the detector, the logical next step would be to adjust the dimensions of the simulated detector and arrange multiple copies of the detector in the same configuration as a full array. If calibration data from GELINA can be obtained, the performance of this array should then be compared to calibration data from the array.

References

[1] International Energy Agency. *World Energy Outlook 2019*. 2019. URL: https://www.iea.org/reports/world-energy-outlook-2019.

[2] United Nations Treaty Collection. *Paris Agreement*. 2016.

[3] V. Masson-Delmotte et al. *IPCC, 2018: Global warming of* $1.5°C$. *AnIPCC Special Report on the impacts of global warming of* $1.5°C$ *above pre-industrial levels and related global greenhouse gas emission pathways, in the context of strengthening the global response to the threat of climate change, sustainable development, and efforts to eradicate poverty*. 2018. URL: https://www.ipcc.ch/sr15/.

[4] World Nuclear Association. *Nuclear Power Reactors*. 2020. URL: https://www.world-nuclear.org/information-library/nuclear-fuel-cycle/nuclear-power-reactors/nuclear-power-reactors.aspx.

[5] World Nuclear Association. *Supply of Uranium*. 2020. URL: https://www.world-nuclear.org/information-library/nuclear-fuel-cycle/uranium-resources/supply-of-uranium.aspx.

[6] World Nuclear Association. *Thorium*. 2017. URL: https://www.world-nuclear.org/information-library/current-and-future-generation/thorium.aspx.

[7] D. Ene et al. "Global characterisation of the GELINA facility for high-resolution neutron time-of-flight measurements by Monte Carlo simulations". In: *Nuclear Instruments and Methods in Physics Research Section A: Accelerators, Spectrometers, Detectors and Associated Equipment* 618.1 (2010), pp. 54–68. ISSN: 0168-9002. DOI: https://doi.org/10.1016/j.nima.2010.03.005. URL: http://www.sciencedirect.com/science/article/pii/S0168900210005589.

[8] Eu Science Hub. *The JRC Neutron Time-of-Flight Facility*. June 2020. URL: https://ec.europa.eu/jrc/en/research-facility/linear-electron-accelerator-facility.

[9] M. Kerveno et al. "From γ emissions to (n,xn) cross sections of interest: The role of GAINS and GRAPhEME in nuclear reaction modeling". In: *European Physical Journal A* 51, 167 (Dec. 2015), p. 167. DOI: 10.1140/epja/i2015-15167-y.

[10] Glenn F. Knoll. *Radiation Detection and Measurement*. New York/Chichester/Weinheim/Brisbane/Toronto/Singapore: John Wiley and Sons Inc., 2000, pp. 353–355.

[11] Glenn F. Knoll. *Radiation Detection and Measurement*. New York/Chichester/Weinheim/Brisbane/Toronto/Singapore: John Wiley and Sons Inc., 2000, pp. 355–356.

[12] Glenn F. Knoll. *Radiation Detection and Measurement*. New York/Chichester/Weinheim/Brisbane/Toronto/Singapore: John Wiley and Sons Inc., 2000, p. 357.

[13] Glenn F. Knoll. *Radiation Detection and Measurement*. New York/Chichester/Weinheim/Brisbane/Toronto/Singapore: John Wiley and Sons Inc., 2000, pp. 365–366.

[14] Glenn F. Knoll. *Radiation Detection and Measurement*. New York/Chichester/Weinheim/ Brisbane/Toronto/Singapore: John Wiley and Sons Inc., 2000, pp. 405–406.

[15] Glenn F. Knoll. *Radiation Detection and Measurement*. New York/Chichester/Weinheim/ Brisbane/Toronto/Singapore: John Wiley and Sons Inc., 2000, pp. 413–414.

[16] Glenn F. Knoll. *Radiation Detection and Measurement*. New York/Chichester/Weinheim/ Brisbane/Toronto/Singapore: John Wiley and Sons Inc., 2000, pp. 408–409.

[17] Glenn F. Knoll. *Radiation Detection and Measurement*. New York/Chichester/Weinheim/ Brisbane/Toronto/Singapore: John Wiley and Sons Inc., 2000, pp. 416–419.

[18] Glenn F. Knoll. *Radiation Detection and Measurement*. New York/Chichester/Weinheim/ Brisbane/Toronto/Singapore: John Wiley and Sons Inc., 2000, pp. 427–430.

[19] Glenn F. Knoll. *Radiation Detection and Measurement*. New York/Chichester/Weinheim/ Brisbane/Toronto/Singapore: John Wiley and Sons Inc., 2000, pp. 308–311.

[20] Reuven Y. Rubinstein. *Simulation and the Monte Carlo Method*. Corporate Headquarters 111 River Street, Hoboken, NJ, USA: Wiley Interscience, 1991, p. 82.

[21] E.R. van der Graaf, P. Dendooven, and S. Brandenburg. "Using standard calibrated geometries to characterize a coaxial high purity germanium gamma detector for Monte Carlo simulations". In: *Rev Sci Instrum.* 85 (May 2014). DOI: doi:10.1063/1.4882320.

[22] GEANT4: A Simulation Toolkit. *Book For Application Developes*. URL: https://geant4.web.cern.ch/support/user_documentation.

[23] AMETEK. *GEM Series Coaxial HPGe Detector Product Configuration Guide*. 801 South Illinois Ave., Oak Ridge, TN 37830 U.S.A., p. 1. URL: https://www.ortec-online.com/products/radiation-detectors/germanium-hpge-radiation-detectors/hpge-radiation-detector-types-how-choose/gem-p-type-coaxial-hpge-radiation-detectors.

[24] S. Agostinelli et al. "GEANT4: A Simulation toolkit". In: *Nucl. Instrum. Meth. A* 506 (2003), pp. 250–303. DOI: 10.1016/S0168-9002(03)01368-8.

[25] Brookhaven National Laboratory. *NuDat2.8*. URL: https://www.nndc.bnl.gov/nudat2/.

[26] *ROOT Data Analysis Framework*. URL: https://root.cern.ch/.

[27] Glenn F. Knoll. *Radiation Detection and Measurement*. New York/Chichester/Weinheim/ Brisbane/Toronto/Singapore: John Wiley and Sons Inc., 2000, pp. 632–633.

[28] National Institute of Standards and Technology. *Critical Values of the Chi-Square Distribution*. URL: https://www.itl.nist.gov/div898/handbook/eda/section3/eda3674.htm.

[29] R.J.H. Klein-Douwel. *Physics Laboratory 1 - Data and Error Analysis*. 2017.

A Error Propagation

Equations used for error propagation come from [29]. These first equations give the relations of the variables.

$$Z = A \pm B \tag{5}$$

$$Z = \frac{A}{B} \ or \ Z = A \cdot B \tag{6}$$

The next two equations give the relations between each variables error for the previous relations, following the same order.

$$\Delta Z = \sqrt{(\Delta A)^2 + (\Delta B)^2} \tag{7}$$

$$\Delta Z = Z \cdot \sqrt{\left(\frac{\Delta A}{A}\right)^2 + \left(\frac{\Delta B}{B}\right)^2} \tag{8}$$

These equations are all that are necessary for the error propagation.

Beginning with the conversion of the peaks from ADC channels to energy, we have an equation of the form

$$E = (p0 \cdot ADC) + p1 \tag{9}$$

where E is the converted peak in units of energy, ADC is the unconverted peak in channel number, and p0 and p1 are the relevant parameters from the calibration curve. Each of these has an associated error. The error in $p0 \cdot ADC$ is given by (8) and the subsequent total error in the energy of the peak ΔE is given by (7), using the error of p1 and the previously calculated multiplication error.

For converting sigma values the following simple equation is used as the sigma values are widths of peaks and so p1 is not used.

$$\sigma_E = p0 \cdot \sigma_{ADC} \tag{10}$$

To find $\Delta\sigma_E$ only (8) is necessary.

The error propagation procedure for the ratios of the sigma and count numbers are the same. As the ratio of two numbers is being taken, (8) can be used in a straightforward manner.

B Raw Fit Data

The following section contains tables of raw data taken from fitting of peaks and any subsequent operations performed on these values.

Table 6: Raw fit data from Eu-152 spectrum

Peak Number	ADC Mean Peak Value	ADC Mean Peak Value Error	ADC Sigma Value	ADC Sigma Error	Count	Count Error
1	6294.786606	0.503099	14.591865	1.042064	4363.609805	163.196892
2	5799.30134	0.143875	13.65314	0.261537	50952.17304	512.139449
3	5347.833404	0.854316	10.290192	1.38396	3482.199369	234.813955
4	5076.142931	1.472508	15.706766	2.843136	1467.033339	204.888576
5	4998.227668	1.139169	16.176308	2.037973	1970.640023	214.377911
6	4583.620638	0.221231	11.366128	0.386351	50230.61478	623.683869
7	4476.643823	0.199453	13.980666	0.552299	39748.69988	511.691538
8	3973.45914	0.167876	12.127552	0.354514	33612.9182	505.433566
9	3575.426127	0.516178	11.43243	2.67033	9096.097699	409.792978
10	3211.975225	0.179977	11.391084	0.336792	29888.4088	520.916026
11	2828.981428	2.068493	6.8131	10.623307	3190.752563	336.184517
12	2350.255705	6.761642	13.120338	1.414127	9353.11829	2666.13144
13	1836.017045	0.421974	11.510023	0.613714	10430.52599	387.007051
14	1702.448897	0.567993	9.47927	0.896318	6364.670267	373.213612
15	1425.798379	0.081656	12.052957	0.145183	112540.0764	869.900754
16	1017.179307	0.202265	10.3028	0.388609	27989.20437	561.821531
17	512.184882	0.101594	9.77866	0.265728	70402.43729	778.4455177

Table 7: Converted fit data from Eu-152 spectrum and matching transition data

Peak Number	Converted Peak Energy (keV)	Converted Peak Error (keV)	Converted Sigma (keV)	Converted Sigma Error (keV)	Matching Transition	Transition Error	Intensity(%)	Intensity Error
1	1531.75	6.74556	3.55184	0.254034	1528.1	4	0.279	3
2	1411.15	6.32635	3.32334	0.0649834	1408.013	3	20.87	9
3	1301.25	5.95602	2.50476	0.337016	1299.142	8	1.633	11
4	1235.12	5.74247	3.82322	0.692216	No Transition	No Transition	No Transition	No Transition
5	1216.16	5.67525	3.93751	0.496308	1212.948	11	1.415	8
6	1115.24	5.33957	2.76665	0.0946671	1112.076	3	13.67	8
7	1089.2	5.25609	3.40306	0.135098	1085.837	10	10.11	5
8	966.715	4.87316	2.95199	0.0870671	963.38/964.057	4/5	26.11	13/7
9	869.829	4.58492	2.78279	0.650082	867.38	3	4.23	3
10	781.36	4.33105	2.77273	0.0826982	778.9045	24	12.93	8
11	688.135	4.11089	1.65839	2.58585	688.67	5	0.856	6
12	571.608	4.13399	3.19365	0.344444	566.438	6	0.131	3
13	446.436	3.52612	2.80168	0.149789	443.9606	16	2.827	14
14	413.924	3.46573	2.30737	0.218362	411.1165	12	2.237	13
15	346.584	3.34722	2.93383	0.0371675	344.2785	12	26.99	20
16	247.121	3.20881	2.50783	0.0951027	244.6974	8	7.55	4
17	124.199	3.09705	2.38024	0.0653524	121.7817	3	28.53	16

Table 8: Raw fit data from simulated Eu-152 Spectrum

Peak Number	Simulated Sigma(keV)	Simulated Sigma Error (keV)	Simulated Count	Simulated Count Error
1	2.541906	0.080314	1183.326479	56.362864
2	2.4986	0.006255	91855.92435	439.474411
3	2.45524	0.028106	7723.576152	144.930567
4	No Transition	No Transition	No transition	No transition
5	2.349033	0.04079	6819.678679	170.409598
6	2.297834	0.008405	70883.47051	431.278828
7	2.265223	0.010682	52762.85934	389.134979
8	2.204393	0.005303	148853.1537	607.825999
9	2.123543	0.017165	26187.83667	317.006362
10	2.059467	0.008019	84869.82593	508.700952
11	2.061123	0.007674	5781.882345	248.909445
12	1.891812	0.063266	1566.781522	254.796556
13	1.832684	0.01549	27162.88109	329.233926
14	1.829961	0.019711	27162.88109	329.233926
15	1.787583	0.002899	312840.862	870.202296
16	1.730298	0.005462	110662.7492	557.637429
17	1.642023	0.001978	569323.0134	1179.156515

Table 9: Raw ratio data for the Eu-152 spectrum

Peak Number	Sigma Ratio	Sigma Ratio Error	Count Ratio	Count Ratio Error
1	1.397313669	0.109256	3.687578942	0.223317
2	1.330080845	0.0262202	0.5546966448	0.00617486
3	1.020169108	0.13776	0.4508532447	0.0315574
4	No Transition	No Transition	No transition	No transition
5	1.676225919	0.213277	0.2889637644	0.0322538
6	1.204025182	0.0414331	0.7086365047	0.00979833
7	1.502306837	0.0600593	0.7533462056	0.0111768
8	1.339139618	0.0396282	0.2258126036	0.00351849
9	1.310446739	0.306314	0.3473405541	0.0162033
10	1.346333784	0.0404959	0.3521676694	0.00649065
11	0.8046050624	1.25459	0.5518535959	0.0628107
12	1.688143431	0.190623	5.969637859	1.95911
13	1.528730539	0.0827471	0.3839992509	0.0149886
14	1.260884795	0.120096	0.2804640483	0.0169414
15	1.641227288	0.0209617	0.3597358596	0.00295522
16	1.449363058	0.0551533	0.2529234505	0.00523441
17	1.449577746	0.0398382	0.1236599182	0.0013911